

Driving unmodeled gravitational-wave transient searches using astrophysical information

P. Bacon,^{1,*} V. Gayathri,² E. Chassande-Mottin,¹ A. Pai,² F. Salemi,³ and G. Vedovato⁴

¹*APC, Université Paris Diderot, CNRS/IN2P3, CEA/Irfu, Observatoire de Paris, Sorbonne Paris Cité, F-75013 Paris, France*

²*Department of Physics, Indian Institute of Technology Bombay, Powai, Mumbai, Maharashtra 400076, India*

³*Max Planck Institute for Gravitational Physics (Albert Einstein Institute), D-30167 Hannover, Germany*

⁴*INFN, Sezione di Padova, I-35131 Padova, Italy*



(Received 11 May 2018; published 16 July 2018; corrected 3 August 2018)

Transient gravitational-wave searches can be divided into two main families of approaches: modeled and unmodeled searches, based on matched filtering techniques and time-frequency excess power identification respectively. The former, mostly applied in the context of compact binary searches, relies on the precise knowledge of the expected gravitational-wave phase evolution. This information is not always available at the required accuracy for all plausible astrophysical scenarios, e.g., in the presence of orbital precession, or eccentricity. The other search approach imposes little priors on the targeted signal. We propose an intermediate route based on a modification of unmodeled search methods in which time-frequency pattern matching is constrained by astrophysical waveform models (but not requiring accurate prediction for the waveform phase evolution). The set of astrophysically motivated patterns is conveniently encapsulated in a graph, that encodes the time-frequency pixels and their co-occurrence. This allows the use of efficient graph-based optimization techniques to perform the pattern search in the data. We show in the example of black-hole binary searches that such an approach leads to an averaged increase in the distance reach (+7–8%) for this specific source over standard unmodeled searches.

DOI: [10.1103/PhysRevD.98.024028](https://doi.org/10.1103/PhysRevD.98.024028)

I. INTRODUCTION

The first gravitational-wave detections made by the advanced LIGO detectors (namely GW150914 [1], GW151226 [2], GW170104 [3] and GW170608 [4]), and recently jointly with advanced Virgo (GW170814 [5], GW170817 [6]), herald a new astronomy which will develop further as more detectors come online such as Kagra [7] and LIGO India [8]. So far, the detections of the gravitational-wave signals associated with the merger of four binary black holes (BBH) [3,9] and a binary neutron star [10] have been announced.

The search for BBH signals in the LIGO/Virgo data is performed using a variety of methods, including the matched filtering technique (such as PyCBC [11], GSTLAL [12] or MBTA [13]). This pattern matching algorithm essentially consists of comparing the data with a waveform model or “template.” The matched filtering BBH searches use a discrete grid of templates. This grid samples the physical parameter space with sufficient density to detect at least 90% of the detectable binary sources (assuming the real signals do not deviate from the

waveform model). The template grid used for the analysis of the first Advanced LIGO run includes $\sim 250,000$ waveforms spanning the compact binaries with total mass $M = m_1 + m_2 < 100 M_\odot$, mass ratio $q = m_1/m_2 < 99$ and the dimensionless spin magnitude < 0.989 [14]. The template grid used for the second Advanced LIGO run has $\sim 400,000$ waveforms covering a parameter space extending to larger masses, $M \lesssim 500 M_\odot$, with a denser sampling in the high-mass region with $q < 3$.

The template waveforms are obtained by solving for the coalescence dynamics during the initial inspiral phase and the merger that follows (for a review, see, e.g., [15]). Current targeted BBH searches use template waveforms obtained from the quadrupolar $(\ell, |m|) = (2, 2)$ gravitational-wave modes emitted by a binary of black holes in quasicircular orbits and with spins aligned to the orbital angular momentum [16].

This model is expected to be a good match with the gravitational-wave emission from binaries formed from isolated star progenitors in galactic fields, but it ignores three effects that can be relevant in other formation scenarios such as dynamical captures in dense stellar environments. The effects so far poorly modeled and/or absent in current searches are higher order than quadrupolar gravitational-

*Corresponding author.
bacon@apc.in2p3.fr

wave modes, orbital precession due to nonaligned spins and orbital eccentricity.

The inclusion of those effects is not straightforward for several reasons. First, gravitational-wave modeling from binaries is still a topic of active research and accurate waveform models are not always available; for instance, this is true for binaries in eccentric orbits [17–19]. Second, a larger search space implies a larger template grid and thus larger computing needs. For instance, the search for an arbitrarily spinning (or “precessing”) binary requires 10 times more template waveforms (order of millions, using relaxed sampling density requirements). The search algorithm also has to be adapted to account for the sky dependency of the signal received by the detector [20].

Current searches based on the quadrupolar aligned-spin quasicircular template waveforms have partial sensitivity to signals that depart from the nominal model. A fraction of the signals can be missed because the signal vs template phase agreement is not good enough to obtain sufficient signal-to-noise ratio, or because the signal is discarded by the “chi-square” consistency test¹ [14,21] applied to reject transient non-Gaussian instrumental noise. A number of studies have evaluated the ability of the current template grids to detect signals departing from the quadrupolar aligned-spin quasicircular model. Depending on the alternative astrophysical model (precession, nonquadrupolar modes, eccentricity) being considered, $\sim 10\%$ to more than 50% of the sources can be missed [20,22–25].

Searching specifically for the aligned-spin quasicircular quadrupolar signals [9] can introduce an observational bias as one is more likely to detect what one has searched for [20]. The sources at or beyond the boundaries of the currently searched parameter space may be of larger interest as they are associated to somewhat unexpected astrophysical scenarios.

Current matched filtering searches will extend in scope, e.g., by including more templates to cover a larger parameter space (see, e.g., [26] for a proposal to cover precessing neutron-star black hole binaries).

In the meantime, the unmodeled transient searches (see, e.g., [27]) provide an alternative approach capable of identifying sources beyond the ones currently addressed by matched filtering. Unmodeled transient searches rely on general assumptions on the target signals instead of a precise model, and detect the signal by identifying power excesses in a time-frequency representation of the data.

The way the power excesses are arranged in the time-frequency plane is directly related to the signal. In this paper, we propose to revisit the pattern matching idea underlying matched filtering searches, and apply this idea to the time-frequency pattern rather than the time- or frequency-domain

waveform. The goal is to improve the sensitivity of existing burst searches by targeting given arrangements or shapes motivated by astrophysical waveform models. This idea is general but we apply it here specifically to one of the major search algorithms referred to as coherent WaveBurst [28], used to analyze LIGO and Virgo data. Similar ideas have been explored in [29–31] in the context of other data analysis pipelines, and in [32] in the context of other searches.

The paper is organized as follows. In Sec. II, we briefly introduce the coherent WaveBurst algorithm. Section III shows how astrophysical models can be encapsulated into a time-frequency graph. This graph is used in a modification of a coherent WaveBurst in order to specialize the search to these particular models. In Sec. IV, we apply this idea to the case of BBH signals and evaluate the sensitivity of the new algorithm using simulated LIGO and Virgo noise. The results are discussed in Sec. V.

II. OVERVIEW OF THE COHERENT WAVEBURST PIPELINE

Coherent WaveBurst (cWB) [28] is a data analysis pipeline used to search for gravitational-wave transients with limited prior knowledge on the waveform. The pipeline has been used to analyze multiple LIGO and Virgo runs. In this section, we review the main steps of cWB.

The data are mapped to the time-frequency domain by using the so-called Wilson-Daubechies-Meyer (WDM) transforms defined in [33]. The WDM transform provides a representation of the data similar to short-term Fourier or Gabor analysis, but it relies on an orthonormal basis composed of regularly distributed sinusoidal functions that we later refer to as “wavelets.” The time and frequency resolutions of this representation are M/f_s and $f_s/(2M)$ respectively, determined by the chosen number M of frequency subbands and the sampling frequency f_s . cWB computes a collection of WDM transforms over a range of time/frequency resolutions to obtain a complete representation of signal features that have different time-scales. Typically, $M = 2^\ell$ for scales $\ell = 4, \dots, 10$ that correspond to analysis timescales ranging from 7.8 ms to 0.5 s when $f_s = 2048$ Hz.

From these collections of WDM transforms cWB only retains the time-frequency pixels that exceed a baseline amplitude which corresponds to the last centile (or per-mille) under Gaussian noise assumption.

Neighboring pixels in time and frequency are grouped in a cluster C . In principle, clusters can have any shape. cWB applies only limits on the cluster shape by fixing the gap between the pixels in time, frequency, and time-frequency. They provide a multiresolution representation of the signal recorded by the considered network of detectors.

Clusters are then characterized using a maximum likelihood ratio statistic obtained from Gaussian noise assumption, assuming the source is at the sky location (θ, ϕ) :

¹This test measures how the amplitude profile of observed signal in the frequency domain differs from that of the closest phase-matching template.

$$L_{\max}(\theta, \phi) = \sum_{p \in C} \mathbf{w}_p^T \mathbf{P}_p \mathbf{w}_p. \quad (1)$$

In the above equation, the sum runs over all pixels p in cluster C . The amplitudes (after whitening) of the time-frequency pixels are collected into a vector $\mathbf{w}_p = \{w_k(t_p - \tau_k(\theta, \phi), f_p, M_p)/S_k^{1/2}(f_p)\}_{k=1, \dots, K}$ where τ_k is the time delay in the arrival time between the k th detector and a fiducial reference point. The time t_p , frequency f_p and scale M_p unequivocally characterize the time-frequency pixel p .

The operator \mathbf{P}_p projects the data into the gravitational-wave subspace spanned by the noise-weighted antenna patterns \mathbf{F}_+ and \mathbf{F}_\times , where $\mathbf{F}_+ = \{F_{k+}(\theta, \phi)/S_k^{1/2}(f_p)\}_{k=1, \dots, K}$ (and similarly for \mathbf{F}_\times) [28]. K defines the number of detectors in the network and $S_k(f)$ is the noise spectral power density for the k th detector.

The sum of the diagonal components of the quadratic form in the summand of Eq. (1) defines the *incoherent energy* E_{in} , while the nondiagonal terms defines the *coherent energy*² E_{coh} , i.e., from signals that are phase-coherent in all detector observations [28].

The energy of the component in the data that does not lie in the gravitational-wave subspace is characterized by the *null energy* [28,34], viz.

$$E_{\text{null}}(\theta, \phi) = \sum_{p \in C} \mathbf{w}_p^T \mathbf{P}_p^{\text{null}} \mathbf{w}_p \quad (2)$$

where $\mathbf{P}_p^{\text{null}} = \mathbf{I} - \mathbf{P}_p$ is the projection operator orthogonal to \mathbf{P}_p .

Those energies inferred from the data are combined into two statistics that characterize the amplitude and consistency of the signal associated with the cluster. The network correlation coefficient $c_c = E_{\text{coh}}/(|E_{\text{coh}}| + E_{\text{null}})$ allows us to distinguish gravitational-wave signals ($c_c \approx 1$) from spurious noise events ($c_c \ll 1$) [28,35]. The statistic $\eta_c = (c_c E_{\text{coh}} K / (K - 1))^{1/2}$ provides an estimate of the network coherent signal-to-noise ratio [28,36].

Depending on the search being performed, other figures of merit are used together with the above two statistics. For instance, to improve background rejection in searches for compact binary coalescences, a selection cut on a crude chirp mass estimate has been introduced (see [37] for details).

III. BASIC PRINCIPLES OF THE PROPOSED METHOD

We now present a new clustering method called Wavegraph for the cWB pipeline. In this section, we explain the general principles and describe the major steps of the algorithm.

²The off-diagonal terms in Eq. (1) do necessarily sum to a positive value for all θ and ϕ . The term “coherent energy” is not always proper.

A. General idea

The proposed method combines three main ingredients. It is based on a formulation of signal detection as pattern matching in the time-frequency plane. An expected pattern is computed from the salient time-frequency pixels, i.e., pixels that stand above the noise level when the signal is detectable.

As detailed in Sec. III B, to compute this characteristic set of pixels we employ an algorithm used for sparse signal approximation that ensures this pixel set contains the complete description of the waveform model.

Astrophysical scenarios generally provide a range of waveforms parametrized by several physical source parameters. For instance, compact binaries are characterized by the binary component masses and spins. This leads to some variability in the expected time-frequency pattern. We encapsulate the waveform model variability into a time-frequency graph; see Sec. III C.

The graphical representation allows us to formulate the detection problem as a combinatorial optimization problem where efficient algorithms can be used, as explained in Sec. III D. In a nutshell, the algorithm seeks the cluster of time-frequency pixels with the largest overall power (more precisely, the incoherent energy carried by the cluster). While matched filtering techniques perform a *global* phase matching over the entire signal, thus requiring a maximum accumulated phase difference between signal and template lower than a fraction of a cycle, this type of search instead performs a *local* phase matching of the signal for each wavelet associated to the pixels in the cluster. This can thus accommodate a phase difference, resulting in more robustness at the expense of some loss of efficiency.

In the following sections we detail all the steps mentioned above. We start from a set of characteristic gravitational signals for the target astrophysical source. In the case of compact binary mergers, we use a template bank employed in matched-filtering-based searches.

B. Sparse signal representation

For each characteristic signal, the first step is to individuate a representative set of salient time-frequency pixels. As mentioned above, the cWB pipeline maps the data to the time-frequency plane using a collection of WDM transforms, that is by projecting the data onto a union of Wilson bases, thus resulting in an overcomplete representation based on a redundant time-frequency dictionary.

Signal expansions in redundant dictionaries are not unique. Sparse linear decompositions provide a complete signal representation where the power is concentrated in a small set of dominating pixels that are thus more likely to stand above the noise level. Because of the small number of pixels, there is a reduced chance that one or several pixels in the decomposition match noisy transients that are often observed in gravitational-wave data.

In an earlier version of the algorithm [38] we proposed to compute the signal expansion from local maxima of the WDM transforms. However, the resulting set of pixels generally failed to ensure full signal energy recovery, thus leading to an overall signal-to-noise ratio loss of 40% on average.

The problem of sparse signal expansion in a redundant dictionary has received a good amount of attention over the last 20 years [39]. Although this problem is non-deterministic polynomial-time (NP)-hard, efficient algorithms are available. The matching-pursuit algorithm [40] is one of these and goes with the following steps:

- (1) Decompose the signal onto the time-frequency dictionary,
- (2) Identify the dictionary wavelet with the largest dot-product,
- (3) Compute the residual signal by subtracting the contribution of the selected wavelet times the associated expansion coefficient.
- (4) Go to step 1 until the residual energy is below a user-defined fraction of the original signal.

In this work, we set the fractional approximation error in the termination condition to $\sim 20\%$. After the first few tenths of iterations (see the bottom panel of Fig. 1), the fractional error decreases slowly with the number of pixels selected for the approximation.³ For instance, choosing 10% instead of 20% error, the number of pixels almost doubles. The extra signal power captured in the graph is distributed over many low-amplitude pixels that only carry a tiny SNR fraction. In the presence of noise, those low-amplitude pixels are largely dominated by noise. In our simulations, the waveform reconstructed from the cluster extracted with the 10% error graph (see Sec. III D) does not improve much, about a 2% increase in SNR. We concluded that a fractional error of 20% is a good compromise.

An example of the sparse decomposition obtained with the matching-pursuit algorithm is shown in Fig. 1. It uses an equal-mass nonspinning BBH signal with $20 M_\odot$ total mass (SEOBNRv2_DoubleSpin model [41]) after whitening by an advanced LIGO design sensitivity curve. The top panel represents the selected time-frequency pixels evidencing the typical raising frequency evolution of gravitational-wave chirp signals. Closer to the final merger, the higher frequencies are captured by the smaller scales (shorter duration wavelets).

The middle panel displays the same signal in the time domain and the approximation obtained by the collection of selected wavelets. The bottom panel shows the norm of approximation error at each iteration. As the number of iterations increases, the error decays slower, thus requiring increasingly more pixels for each percent improvement.

³This is a well-known behavior of the matching-pursuit algorithm; see [39].

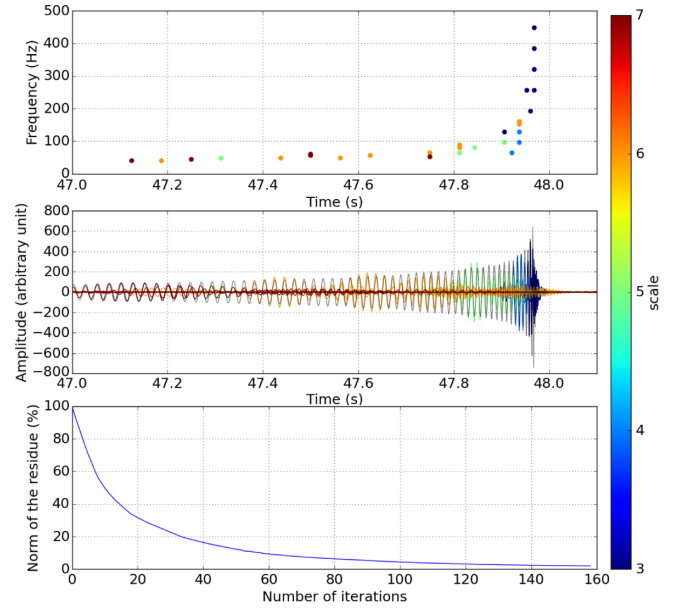


FIG. 1. Convergence of the matching-pursuit algorithm in the case of an equal-mass nonspinning BBH waveform with $20 M_\odot$ total mass after whitening by advanced LIGO design sensitivity power density spectrum (PSD). Fixing the termination condition at 20% collects 33 pixels and ensures sparsity (bottom). Time-frequency pixels are selected by the matching-pursuit algorithm (top) and corresponding wavelets (middle) for the very same signal. The color indicates the scale ℓ associated to each pixel that corresponds to wavelet timescales $2^\ell / f_s$. Strain amplitude of the original waveform (black) is shown in the background. Some early time pixels are not displayed that are selected by the matching pursuit.

C. Graph computation

The set of time-frequency pixels selected by the sparse signal approximation provides a compact representation of the waveform model. With the selected pixels, we form a cluster by connecting pixels to keep a record of their co-occurrence in association to the same signal. To limit the number of interconnections we only connect pixels that are adjacent in a particular ordering defined by a rule, e.g., by ascending order in time first, and ascending in frequency second. This thus forms a chain where a pixel is connected to one pixel downstream and another upstream.

We repeat this operation for different alignments in time between the waveform and the coarsest time-frequency lattice associated to the WDM transform with the largest analysis timescale. These alignments are obtained by shifting the waveform in time by multiples of the smallest analysis timescale. For the scale range $\ell = 3, \dots, 7$ used here, there is thus a maximum of $2^4 = 16$ possible alignments.

We also repeat this operation on every waveform associated with the considered astrophysical scenario, i.e., the template bank. We thus obtain as many pixel clusters as there are templates in the bank times the number of alignments.

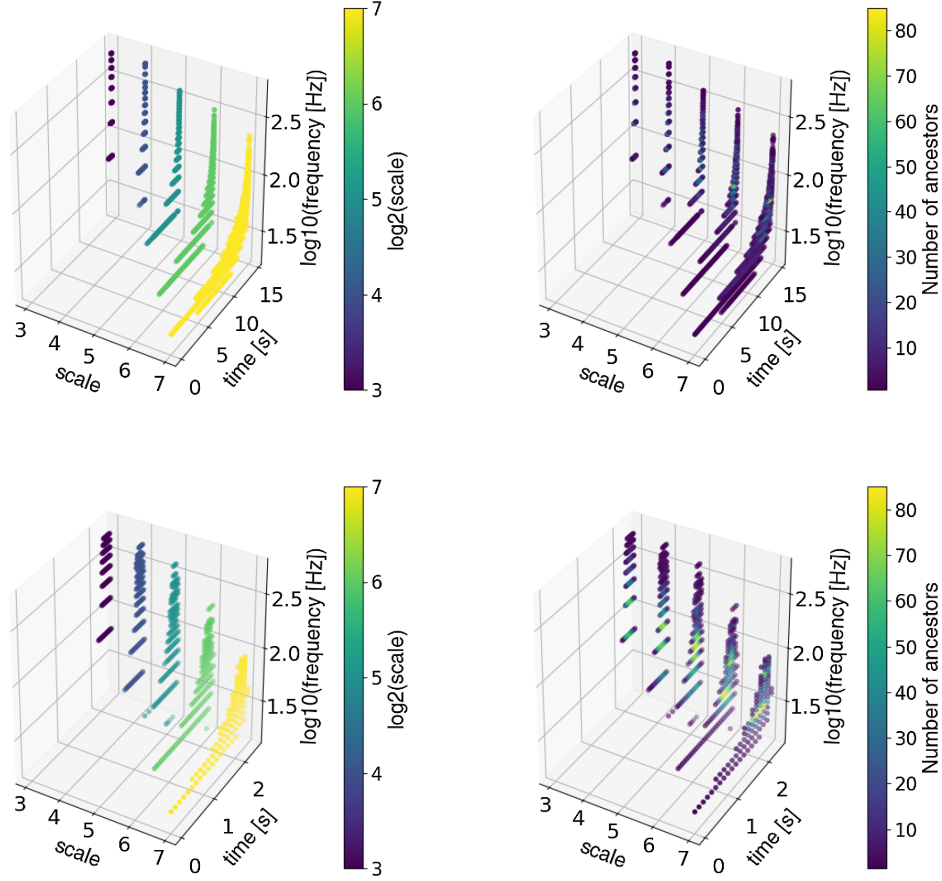


FIG. 2. Time-frequency graphs used to search for BBH signals with the Wavegraph algorithm: R1 region (top) and R2 (bottom). The number of ancestors refers to the number of edges linking a given pixel to its neighbors that precede that pixel in the selected pixel ordering. It is an indicator of the graph complexity.

The pixels in the clusters are characterized by the central time, frequency and duration of their corresponding wavelet. The connections between pixels form a time-frequency graph. As two clusters may have pixels in common, pixels in the intersection receive the connections they have in the two clusters of origin. They thus end up being connected to more than one pixel downstream or upstream. The graph is oriented and acyclic, for a well-chosen pixel ordering rule.

The resulting graph provides a compact and convenient representation of the entire waveform manifold associated with an astrophysical scenario. It allows us to use efficient search algorithms borrowed from graph-based combinatorial optimization as we will see in the next section.

We provide examples of graphs produced for BBH searches in Sec. IV (see Fig. 2).

D. Search observational data using the graph

Signals from the targeted family can be searched by finding the cluster C^* in the graph that maximizes the likelihood ratio in Eq. (1). However this would require the computation of L_{\max} over the sky coordinates which is too computationally expensive. Instead we identify the inter-connected cluster in the graph G that satisfies

$$C^* = \arg \max_{C \in G} \sum_{p \in C} E_p - \lambda \bar{E}(f_p, M_p), \quad (3)$$

where $E_p = \sum_k \hat{w}_{p,k}^2$ with

$$\hat{w}_{p,k}^2 = \max_{\theta, \phi} w_k^2(t_p - \tau_k(\theta, \phi), f_p, M_p). \quad (4)$$

The first part of the sum in (3) is a proxy for the likelihood ratio in (1). Though not identical, the term E_p is related to the incoherent energy E_{in} introduced earlier in Sec. II. $\bar{E}(f_p, M_p)$ is an estimate of the noise level at a given f_p and M_p obtained by the median value of E_p at this frequency and scale for all times.

The second term of the summation in (3) is a kind of “Occam’s razor” penalization term that favors small clusters. Without this penalization, the maximization in (3) would have the tendency to prefer large clusters that accumulate more noise power than smaller signal-related clusters. The factor λ allows us to tune the strength of this penalization. Typically, we set $\lambda = 1$.

Maximizing Eq. (3) can be directly related to the class of “longest path problem” and can be solved by the dynamic

programming algorithm. The computational cost scales linearly with the number of connections in the graph. This makes it particularly efficient even for complex graphs.

When applying the search to a segment of observational data, this segment is divided into successive blocks shifted by strides equivalent to the largest analysis timescale. The best-fit cluster C^* is computed in all blocks.

The follow-up of the selected clusters is performed following the standard cWB workflow, by computing their coherent statistics c_c and η_c given in Sec. II. We measured that the use of this clustering algorithm in cWB results in an execution time about 20% larger compared to a standard cWB on the same computer.

IV. RESULTS

While this method is applicable in principle to a broad range of astrophysical models, we will use the specific case of compact binary mergers to demonstrate the idea. In this section we show how Wavegraph can improve upon cWB in searching for BBH signals in simulated Gaussian noise. We give a comparison with the recent version of cWB that was used in [3].

A. Time-frequency graphs

We carry out simulations of a BBH search using cWB with and without Wavegraph. In order to check the effect of using graphs with different size and complexity we divided the mass range into two disjoint regions.

The region R1 (low-mass) corresponds to a total mass range of $10 - 25 M_\odot$, while R2 (higher mass) covers $40 - 70 M_\odot$. The selected range of masses is similar to that of the BBH events observed during the first two LIGO observational runs. For both regions, we set the mass ratio $q = m_2/m_1 \leq 2$ and cover the entire spin range available for the waveform model SEOBNRv2_ROM_DoubleSpin [42–44] up to almost maximally spinning black holes.

Using the algorithm described in Sec. III C we compute the time-frequency graphs using grids of template waveforms that cover the mass range chosen for each region.

We used template grids of 28 201 (2 950) waveforms for the R1 (R2) region computed using a stochastic placement algorithm [45]. To limit the overall computational cost for the time-frequency graph, the set of template waveforms is produced with a slightly coarser sampling of the parameter space in the R1 case (minimal match of 95% for the R1 graph, and 99% for R2) and used a limited number of waveform alignments; only 1 for R1, and 32 for R2.

This leads to a graph with 1643 pixel nodes for R1, and 941 nodes for R2, a difference that can be explained by the relatively shorter signal duration for higher-mass binaries in R2.

The top left panel of Fig. 2 displays the pixels in the graph computed for R1 and R2 with time on the x -axis, frequency on the y -axis and scale encoded in colors. The

panel on the right shows the graph connectivity, i.e., the number of connections of a given time-frequency pixel with its neighbors.

As expected, the overall graph time support and complexity is larger for R1 as the BBH signals have a longer duration for this mass range and there is a higher density of template waveforms.

We thus perform two searches using cWB with Wavegraph and the R1 and R2 graphs separately. We do not intend to combine the two searches *a posteriori* (which would then require us to apply a trial factor to account for the multiple search attempts). The idea is rather to show how the search background changes with the different graphs.

B. Simulated data set

We present a Monte Carlo simulation of the three-detector network composed of the two LIGO and the Virgo detectors. We used simulated Gaussian noise colored according to the advanced LIGO and Virgo design sensitivities given in [46,47].

We simulate and add about 10^6 signals from binaries that are arbitrarily oriented, isotropically and uniformly distributed in volume up to maximum (luminosity) distances of 1.4 and 3 Gpc for the R1 and R2 analysis respectively. These limits are much larger than the search distance reach. The source sample thus includes many low SNR binaries, a majority of which are below the detection threshold. This allows us to correctly estimate the sensitive distance.

Cosmological effects are ignored in this simulation. The binary population is thus not exactly distributed uniformly in a comoving volume. We expect this to have little impact on the final result as we are primarily interested in the *relative* sensitivity improvement between pipelines and the bulk of the detected sources is located at low- $z < 0.1$.

The mass ranges of the simulated signals are consistent though slightly larger than the span used to compute the time-frequency graph. A small fraction of the injected signals may then fall outside of the time-frequency graph mass coverage.

C. Results

In this section, we summarize the main results obtained running the Monte Carlo simulation presented in the previous section.

1. Background estimation

We compare the search algorithm sensitivities at a fixed false-alarm rate (FAR). We evaluate the false-alarm rate by generating 129 days of simulated Gaussian noise for the three detectors. We then follow the background estimation procedure classically used for actual searches. It is based on surrogate data produced by applying nonphysical time shifts (larger than time of flight between detectors) [36]. By applying this procedure to the original data set with

~ 600 time lags, we generate the equivalent of 212 years of time-shifted surrogate data. The analysis of this noise-only data results in the search background, i.e., a set of noise-related events each characterized by their statistics η_c and c_c defined in Sec. II. The search background is further used to associate a FAR estimate to any detected signals by counting the number of background events passing the same selection cuts. The FAR estimate is a measure of the event significance, i.e., the probability for an event to come from the noise.

We apply selection cuts similar to that used in actual searches. These include the ones introduced for the rejection of transient noise (or glitches) present in the LIGO and Virgo data, although this type of noise is not present in the simulated data used for this study. Signals with a low network correlation coefficient c_c are discarded (poor phase coherence between pairs of detectors). We have used $c_c = 0.7$ for both analyses.

Clusters of pixels associated with only few wavelet durations (or time-frequency resolutions) are also discarded as this type of cluster is not representative of what is expected for BBH signals (see Sec. III B and Fig. 1). The cWB analysis includes a third selection cut based on a chirp mass estimate obtained from the reconstructed time-frequency pattern (see [27] for details). This selection retains clusters that possess a “chirping-up” time-frequency signature compatible with BBH signals.

Figure 3 represents the cumulative distribution of the background as a function of the ranking statistic η_c . Both analyses using Wavegraph have a higher background rate than cWB alone. Our explanation is that the clusters extracted using Wavegraph are, by design, larger on average and with a wider spread in time. Also, while

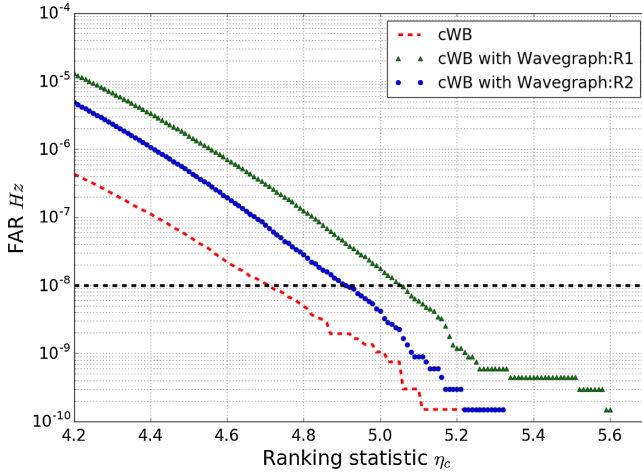


FIG. 3. Cumulative distribution of background events vs the statistic η_c for cWB red/dashed line, with cWB with Wavegraph using the R1 graph (green/triangle line) and R2 graph (blue/square line). The dotted line shows the reference FAR of 10^{-8} Hz = 0.3 event/yr, chosen to compare the different pipelines.

cWB gathers sets of contiguous pixels with large amplitudes, Wavegraph allows for interruption, since the cluster is selected whenever the overall energy evaluated globally is large whether the cluster is a connected set or not. These two effects have the consequence to slightly expand the signal space accessible to Wavegraph.

The analysis using the R1 graph has a higher background compared to R2. We relate this to the increase in size and complexity of the graph, that has about twice the number of nodes in the R1 case, which thus increases the probability of picking up noise outlier.

At the reference FAR = 10^{-8} Hz (0.3 event/yr) adopted here, we obtain the η_c selection threshold of 4.7, 4.9 (+4%) and 5.05 (+5%) for cWB, cWB with Wavegraph (R1) and cWB with Wavegraph (R2) respectively. We estimate the accuracy on the determination of those thresholds to be $\lesssim 0.6\%$. In the following, we apply this selection threshold on η_c to declare a signal detected.

Since this ranking statistic is homogeneous to the signal-to-noise ratio and is thus inversely proportional to the distance, we may conclude that one loses a few percent of distance reach by using Wavegraph. This conclusion is however not correct as it does not fold in the amount of SNR recovered on average in the presence of a real signal as we will see in the next section.

2. Signal recovery

In this section we examine the average properties of the BBH signals from the injection population that are detected by cWB and cWB with Wavegraph.

Table I tabulates the summary of injected and recovered BBH signals in both R1 and R2 regions by cWB with and without Wavegraph. The numbers show the percentage improvement in recovery with and without Wavegraph. About 35–40% of the events recovered with Wavegraph are missed by cWB alone (exactly 14627 and 11402 for the R1 and R2 regions respectively). Conversely, 15–25% of the events recovered by cWB alone are missed when using Wavegraph (exactly 7941 and 4492 for the R1 and R2 regions respectively). There is thus a good complementarity.

In Fig. 4 we display the detection efficiency (percent) vs the injected network SNR for cWB and cWB with Wavegraph. For the two mass regions, the results shows that the use of Wavegraph improves the detection efficiency

TABLE I. Number of injected/recovered signals by the simulation in the R1 and R2 regions for the two compared pipelines. Note the recovered signals indicated in the table are not exclusive to a single pipeline.

Algorithm	R1 region		R2 region	
	Injected	Recovered	Injected	Recovered
cWB	930 744	28 900 (3.1%)	930 870	26 927 (2.9%)
cWB with Wavegraph	930 744	35 340 (3.8%)	930 870	33 699 (3.6%)

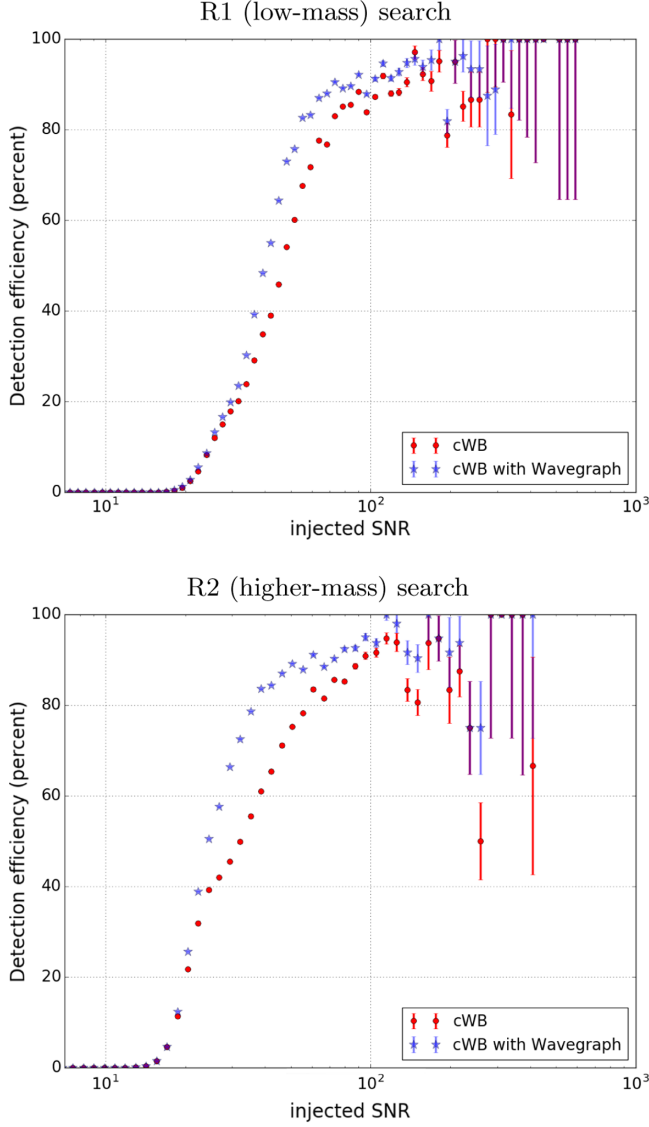


FIG. 4. Detection efficiency (percent) vs the injected network SNR given for cWB in red circles and for cWB with Wavegraph in blue stars with 1-sigma error bars. The top and bottom panels correspond to the R1 and R2 simulations respectively.

especially in the low injected network SNR region, though we applied a more selective threshold on η_c to keep the FAR requirement equal for all searches.

In Fig. 5 we show the distribution of the network correlation c_c statistic for the signals recovered by cWB (red/darker) and with Wavegraph (blue/lighter). It appears that using Wavegraph, the recovered signals have a higher c_c statistic for both R1 and R2 searches. Thanks to the information extracted from the waveform model stored in the time-frequency graph, the Wavegraph algorithm is more likely to pick pixels relevant to the gravitational-wave signal, leading to an overall larger correlation.

We estimate the distance reach by computing the sensitivity distance within which we would be able to detect a signal, averaged over the observation time and over

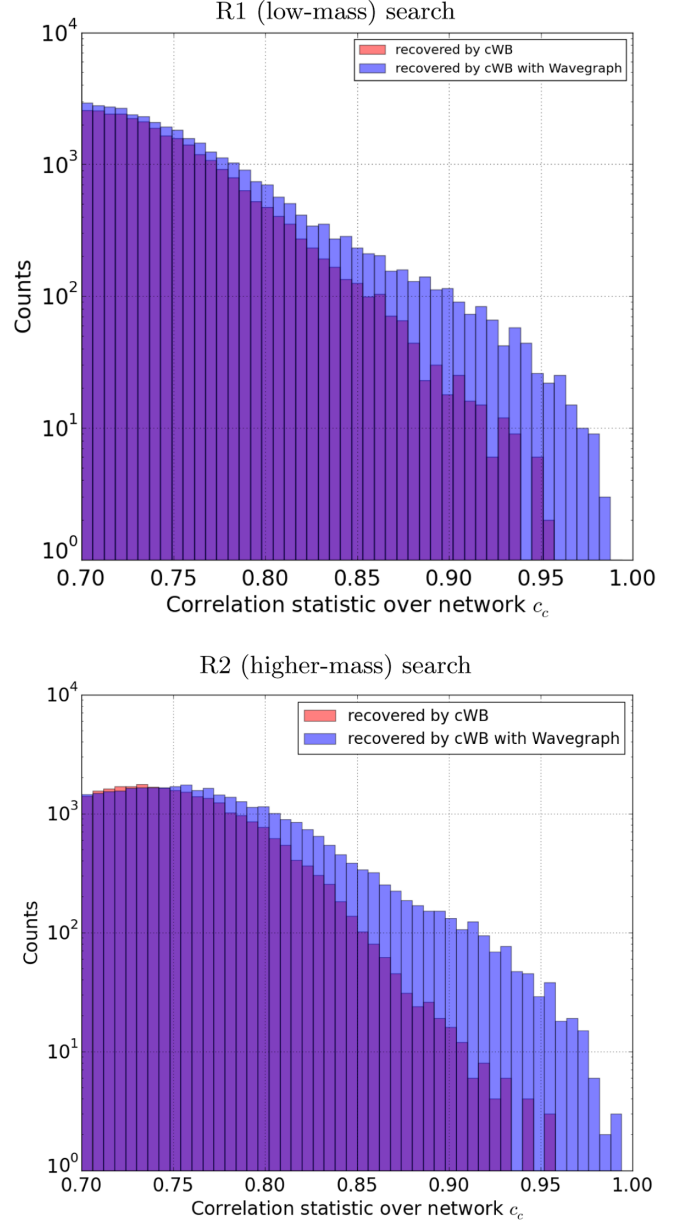


FIG. 5. Histograms of the network correlation coefficient of recovered events by the R1 (top panel) and R2 (bottom panel) simulations. Both show the counts for cWB (red/darker) and cWB with Wavegraph (blue/lighter). Wavegraph is on average reconstructing events with a greater correlation over the network. The effect tends to be even more pronounced with louder injections.

source sky location and orientation [48]. We checked that this distance scales as expected with $\mathcal{M}^{5/6}$ where $\mathcal{M} = (m_1 m_2)^{3/5} / (m_1 + m_2)^{1/5}$ is the chirp mass.

Figure 6 displays the relative improvement in the sensitive distance for various mass bins for the R1 (top) and R2 (bottom) regions. In the R1 region, the average relative improvement in sensitive distance when using cWB with Wavegraph is $\sim 7\%$ with a maximum of 9.7% for asymmetric binaries ($q \sim 2$). In the R2 region, the average

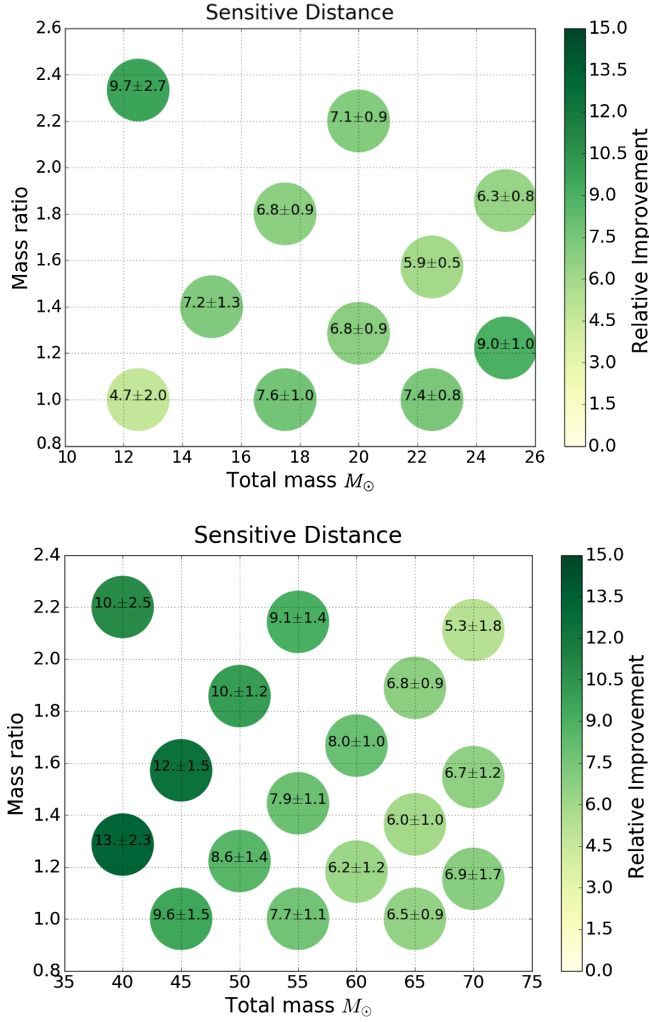


FIG. 6. Relative sensitive distance improvement (in percent) when using cWB with Wavegraph with respect to cWB alone for R1 (top panel) and R2 (bottom panel). The color scale encodes the importance of the improvement with respect to cWB alone.

improvement is $\sim 8\%$ with a maximum at 13% in the lower part of this mass range. Overall, this translates into an improvement in the event of about 20–25% at a FAR level of 0.3/yr. We observe that the improvement in the sensitive distance decreases with the total mass for a fixed mass ratio. As the total mass increases, the BBH chirp signal shortens and cWB is able to collect all relevant pixels. The dependencies of the relative sensitive distance improvement with the mass ratio, for a fixed total mass, are rather weak.

V. CONCLUSIONS

In this work we show that it is possible to improve the sensitivity of the time-frequency pattern search algorithms used in the context of unmodeled gravitational-wave transient searches, such as cWB, by restricting the exploration to patterns obtained from astrophysical waveform models.

We propose a pattern matching algorithm called “Wavegraph” that we implemented as a module in the cWB search pipeline. The algorithm has no significant impact on the overall computational cost of the search.

We applied and tested this algorithm for the case of BBH signals, and this leads to an averaged 7–8% improvement in the standard cWB distance reach over the considered mass range (total mass of 10 – 70 M_\odot). This translates into a 20–25% relative improvement in the detection rate, assuming an isotropic source distribution. We attribute this enhancement to the more efficient collection of signal-related time-frequency pixels achieved by the proposed algorithm. Our tests evidence the impact of the graph size on the background level and search sensitivity.

The method is an intermediate approach between matched-filtering-based searches that rely on the precise knowledge of the signal phase evolution and unmodeled searches that impose little priors. We consider the method particularly adapted to areas of the compact binary space such as high-mass ratio binary and precessing or eccentric orbital evolution, where it is difficult to build an exhaustive template bank thus preventing standard modeled searches to operate.

This method is general and applies to a broad range of situations, including the cases where only numerical waveform models (e.g., from numerical relativity simulations) are available.

Similarly to cWB, the Wavegraph algorithm is sensitive to instrumental and/or environmental transient noise. In a follow-up article, we assess the impact of real detector noise on the search and develop an additional glitch rejection scheme allowed by the time-frequency graph to circumvent this issue [49].

ACKNOWLEDGMENTS

This research was supported by the CEFIPRA Grant No. IFC/5504, by the European Union’s Horizon 2020 research and innovation program under Grant No. 653477, by the French Agence Nationale de la Recherche (ANR) under reference ANR-15-CE23-0016 (Wavegraph project), and by CNRS PICS/Inde. V.G. acknowledges Inspire division, DST, Government of India for the fellowship support. V.G. would like to thank IISER-TVM for providing the facility to complete the initial part of this work. V.G. thanks the Max Planck Partner Group on Gravitational Waves grant for the travel support to Albert Einstein Institute. The authors are grateful to the LIGO Scientific Collaboration and Virgo Collaboration for giving access to the simulation software used here, and specifically to the cWB team for their help and support. The authors are grateful to Sergey Klimenko, Marco Drago, Stéphane Jaffard, and Aurélia Fraysse for their valuable comments and suggestions.

- [1] B. P. Abbott *et al.* (LIGO Scientific Collaboration and Virgo Collaboration), *Phys. Rev. Lett.* **116**, 061102 (2016).
- [2] B. P. Abbott *et al.* (LIGO Scientific Collaboration and Virgo Collaboration), *Phys. Rev. Lett.* **116**, 241103 (2016).
- [3] B. P. Abbott *et al.* (LIGO Scientific Collaboration and Virgo Collaboration), *Phys. Rev. Lett.* **118**, 221101 (2017).
- [4] B. P. Abbott *et al.* (LIGO Scientific Collaboration and Virgo Collaboration), *Astrophys. J. Lett.* **851**, L35 (2017).
- [5] B. P. Abbott *et al.* (LIGO Scientific Collaboration and Virgo Collaboration), *Phys. Rev. Lett.* **119**, 141101 (2017).
- [6] B. P. Abbott *et al.* (LIGO Scientific Collaboration and Virgo Collaboration), *Phys. Rev. Lett.* **119**, 161101 (2017).
- [7] Y. Aso, Y. Michimura, K. Somiya, M. Ando, O. Miyakawa, T. Sekiguchi, D. Tatsumi, and H. Yamamoto (KAGRA Collaboration), *Phys. Rev. D* **88**, 043007 (2013).
- [8] B. Iyer *et al.*, Technical Report No. M1100296-v2 (LIGO-India, 2011), <https://dcc.ligo.org/1248/LIGO-M1100296/public>.
- [9] B. P. Abbott *et al.* (LIGO Scientific Collaboration and Virgo Collaboration), *Phys. Rev. X* **6**, 041015 (2016).
- [10] B. Abbott *et al.* (LIGO Scientific Collaboration and Virgo Collaboration), *Phys. Rev. Lett.* **119**, 161101 (2017).
- [11] S. A. Usman *et al.*, *Classical Quantum Gravity* **33**, 215004 (2016).
- [12] S. Privitera, S. R. P. Mohapatra, P. Ajith, K. Cannon, N. Fotopoulos, M. A. Frei, C. Hanna, A. J. Weinstein, and J. T. Whelan, *Phys. Rev. D* **89**, 024003 (2014).
- [13] T. Adams, D. Buskulic, V. Germain, G. M. Guidi, F. Marion, M. Montani, B. Mours, F. Piergiovanni, and G. Wang, *Classical Quantum Gravity* **33**, 175012 (2016).
- [14] B. P. Abbott *et al.* (LIGO Scientific Collaboration and Virgo Collaboration), *Phys. Rev. D* **93**, 122003 (2016).
- [15] S. A. Hughes, *Annu. Rev. Astron. Astrophys.* **47**, 107 (2009).
- [16] T. Dal Canton and I. W. Harry, [arXiv:1705.01845](https://arxiv.org/abs/1705.01845).
- [17] T. Damour, A. Gopakumar, and B. R. Iyer, *Phys. Rev. D* **70**, 064028 (2004).
- [18] S. Tanay, M. Haney, and A. Gopakumar, *Phys. Rev. D* **93**, 064031 (2016).
- [19] B. Moore, M. Favata, K. G. Arun, and C. K. Mishra, *Phys. Rev. D* **93**, 124061 (2016).
- [20] I. Harry, S. Privitera, A. Bohé, and A. Buonanno, *Phys. Rev. D* **94**, 024012 (2016).
- [21] B. Allen, *Phys. Rev. D* **71**, 062001 (2005).
- [22] J. Calderón Bustillo, S. Husa, A. M. Sintes, and M. Pürrer, *Phys. Rev. D* **93**, 084019 (2016).
- [23] V. Varma, P. Ajith, S. Husa, J. Calderon Bustillo, M. Hannam, and M. Pürrer, *Phys. Rev. D* **90**, 124004 (2014).
- [24] C. Capano, Y. Pan, and A. Buonanno, *Phys. Rev. D* **89**, 102003 (2014).
- [25] E. Huerta *et al.*, *Phys. Rev. D* **95**, 024038 (2017).
- [26] N. Indik, K. Haris, T. Dal Canton, H. Fehrmann, B. Krishnan, A. Lundgren, A. B. Nielsen, and A. Pai, *Phys. Rev. D* **95**, 064056 (2017).
- [27] B. P. Abbott *et al.* (LIGO Scientific Collaboration, Virgo Collaboration), *Phys. Rev. D* **93**, 122004 (2016).
- [28] S. Klimenko *et al.*, *Phys. Rev. D* **93**, 042004 (2016).
- [29] M. Coughlin, P. Meyers, E. Thrane, J. Luo, and N. Christensen, *Phys. Rev. D* **91**, 063004 (2015).
- [30] E. Thrane and M. Coughlin, *Phys. Rev. D* **89**, 063012 (2014).
- [31] M. Coughlin, E. Thrane, and N. Christensen, *Phys. Rev. D* **90**, 083005 (2014).
- [32] S. Suvorova, L. Sun, A. Melatos, W. Moran, and R. J. Evans, *Phys. Rev. D* **93**, 123009 (2016).
- [33] V. Necula, S. Klimenko, and G. Mitselmakher, *J. Phys. Conf. Ser.* **363**, 012032 (2012).
- [34] P. J. Sutton, G. Jones, S. Chatterji, P. Kalmus, I. Leonor, S. Poprocki, J. Rollins, A. Searle, L. Stein, M. Tinto, and M. Was, *New J. Phys.* **12**, 053034 (2010).
- [35] S. Klimenko, I. Yakushin, A. Mercer, and G. Mitselmakher, *Classical Quantum Gravity* **25**, 114029 (2008).
- [36] B. P. Abbott *et al.* (LIGO Scientific Collaboration and Virgo Collaboration), *Phys. Rev. Lett.* **116**, 131103 (2016).
- [37] V. Tiwari, S. Klimenko, V. Necula, and G. Mitselmakher, *Classical Quantum Gravity* **33**, 01LT01 (2016).
- [38] E. Chassande-Mottin, E. Lebigot, H. Magaldi, E. Chase, A. Pai, V. Gayathri, and G. Vedovato, [arXiv:1710.09256](https://arxiv.org/abs/1710.09256).
- [39] S. Mallat, *A Wavelet Tour of Signal Processing: The Sparse Way*, 3rd ed. (Academic Press, Burlington, MA, 2009).
- [40] S. Mallat and Z. Zhang, *IEEE Trans. Signal Proc.* **41**, 3397 (1993).
- [41] M. Pürrer, *Phys. Rev. D* **93**, 064041 (2016).
- [42] A. Taracchini, Y. Pan, A. Buonanno, E. Barausse, M. Boyle, T. Chu, G. Lovelace, H. P. Pfeiffer, and M. A. Scheel, *Phys. Rev. D* **86**, 024011 (2012).
- [43] A. Taracchini *et al.*, *Phys. Rev. D* **89**, 061502 (2014).
- [44] M. Pürrer, *Phys. Rev. D* **93**, 064041 (2016).
- [45] I. W. Harry, B. Allen, and B. S. Sathyaprakash, *Phys. Rev. D* **80**, 104014 (2009).
- [46] J. Aasi *et al.* (LIGO Scientific Collaboration), *Classical Quantum Gravity* **32**, 074001 (2015).
- [47] F. Acernese *et al.* (Virgo Collaboration), *Classical Quantum Gravity* **32**, 024001 (2015).
- [48] J. Aasi *et al.*, *Phys. Rev. D* **87**, 022002 (2013).
- [49] V. Gayathri *et al.* (to be published).

Correction: The lower panel of the previously published Fig. 6 contained an error and its corrected replacement has been posted.